Research Square

Preprints are preliminary reports that have not undergone peer review.
They should not be considered conclusive, used to inform clinical practice,
or referenced by the media as validated information.

Machine learning prediction of hydrogen sorption properties of zirconium-titanium based C14 Laves phase AB 2 alloy from chemical composition

Suwarno Suwarno

warno@me.its.ac.id

Institut Teknologi Sepuluh Nopember (ITS)

Mohammad Ismail

Universiti Malaysia Terengganu

witantyo Witantyo

Institut Teknologi Sepuluh Nopember (ITS)

Ivan Tolj

University of Split

Article

Keywords:

Posted Date: November 2nd, 2026

DOI: https://doi.org/10.21203/rs.3.rs-10703459/v1

License: This work is licensed under a Creative Commons Attribution 4.0 International License.
Read Full License

Additional Declarations: No competing interests reported.

Machine learning prediction of hydrogen sorption properties of zirconium-titanium based C14 Laves phase AB_2 alloy from chemical composition

S. Suwarno[a,*], M. Ismail[b], Witantyo[a], I. Tolj[c]

[a]*Department of Mechanical Engineering, Institut Teknologi Sepuluh Nopember (ITS), Surabaya 60111, Indonesia*
[b]*Energy Storage Research Group, Faculty of Ocean Engineering Technology and Informatics, Universiti Malaysia Terengganu, 21030 Kuala Nerus, Malaysia*
[c]*Faculty of Electrical Engineering, Mechanical Engineering and Naval Architecture, University of Split, Rudjera Boskovica 32, Split 21000, Croatia*

Abstract

Machine learning (ML) models were developed to predict the hydrogen sorption properties of Zr–Ti-based C14 Laves phase AB_2 alloys—unit cell volume (V14), enthalpy of hydrogen absorption (ΔH), entropy of hydrogen absorption (ΔS), and equilibrium plateau pressure (P_{eq})—from chemical composition and calculated physical properties. A curated dataset of 244 alloys was compiled from the literature, with two feature categories compared: element atomic percent and properties-based variables (molar mass, bulk density, molar volume, atomic radius ratio, bulk modulus, electron density, B/A ratio). Five ML algorithms (linear regression, random forest, ridge regression, KNN, XGBoost) were trained with 80/20 train–test split, 5-fold cross-validation, and forward feature selection. Element atomic percent features outperformed properties-based features for all target variables. V14 was predicted with the

*Corresponding author
Email address: warno@me.its.ac.id (I. Tolj)

highest accuracy (R^2 up to 0.955 on the test set), while P_{eq} showed moderate accuracy (R^2 up to 0.741) and a notable linear correlation with V14. Prediction of ΔH and ΔS yielded moderate and low accuracies, respectively, highlighting opportunities for more advanced feature engineering. These results demonstrate the potential of ML to accelerate the design of AB_2 hydrogen storage alloys.

Keywords: AB_2 alloy, C14 Laves phase, Hydrogen storage, Machine learning, Feature selection, Zirconium-titanium

1. Introduction

Metal hydrides are compounds of metallic elements with hydrogen. Due to their reversible formation and dissociation, metal hydrides can be used for various energy storage applications, including solid-state hydrogen storage for automotive applications [1] and as electrode materials in nickel–metal hydride (NiMH) batteries [2].

Metal hydrides can be classified into three classes, each with distinct attributes. The first class is binary hydrides, in which metals absorb hydrogen in their lattice sites to form metal–hydrogen compounds (e.g., MgH_2, CaH_2). Hydrides of Groups I and II metals exhibit ionic metal–hydrogen bonding, with the exception of MgH_2, which represents a transition between ionic and metallic hydride. The binary hydrides of transition metals (d-block) are metallic in properties and appearance. Alloys can form with either disordered or ordered crystal structures; the former are called solid solution alloys, whose hydrides belong to the BCC-based hydride class (e.g., Ti–V alloys) [3, 4, 5]. The latter are intermetallic alloys with ordered crystal structures, typically

C14 and C15 Laves phase types [6], whose hydrides constitute the intermetallic hydride class. The last class is complex hydrides, which are compounds of metals (notably Groups I and II) with hydride complexes of the boron family.

Titanium-based metal hydrides belong to an important class because of their unique properties, abundance, and relatively low cost. The volumetric hydrogen density of TiH_2 is 150 kg H_2/m^3, more than twice that of liquid hydrogen. The formation enthalpy of TiH_2 is -123.4 kJ/mol H_2 at 298 K, meaning significant heat is released during hydrogenation, making Ti and its alloy hydrides candidates for heat storage systems. The high stability of TiH_2, with a dissociation temperature of approximately 700 °C at 1 bar, makes these alloys potentially interesting as high-temperature hydrogen storage materials. The interaction of hydrogen with vanadium is rather complex, with various stable vanadium hydrides forming below approximately 200 °C. Ti–V alloys absorb about 4 wt.% hydrogen, and their kinetics and thermal stability can be tuned by alloying and microstructure control [3, 4, 7]. Although the crystal structure is BCC in most of these cases, the addition of extra elements may result in the formation of a secondary C14 phase.

Among the intermetallic hydrides, AB_2-type alloys have received considerable attention because of their high hydrogen capacities compared with AB_5-type intermetallics, along with their easy activation [8, 9]. In the A–B systems, three individual phases are formed, including two Laves-type intermetallics with a hexagonal C14 ($MgZn_2$-type) and cubic C15 (Cu_2Mg-type) structure. Hydrogen storage capacities, thermodynamics, and kinetics of the formed hydrides are affected by the fraction of each phase [10]. C14 and C15

type compounds normally have lower capacities than the BCC alloy; however, the C14 or C15 structures have advantages in sustaining cycle stability and possess improved activation properties. Recent interest lies in using less pure elements for preparing the alloy to reduce overall cost, for example using Fe–V instead of pure V and Fe [11, 12].

Machine learning is now widely used in materials science studies [13, 14, 15, 16, 17]. The first and most crucial step is data gathering and data treatment so that the sample can be used to accurately predict the properties. Selection of the learning algorithms depends on the aim of the research. Recently, some works have used machine learning approaches to predict the properties of metal hydrides [18, 19]; however, the databases used are quite old, and updating the database is useful. More recent studies have applied ML to AB_2 alloys specifically [20, 21, 22, 23], hydrogen storage capacity estimation [24, 25], thermodynamic property prediction [26], and high-entropy Laves phase hydride exploration [27, 28]. Zhang et al. [29] applied machine learning to predict formation enthalpies of intermetallics, demonstrating the viability of data-driven approaches for Laves phase compounds. Dedicated hydrogen storage material databases and AI-assisted literature mining platforms have also been developed [30], and ML-augmented data augmentation approaches have been applied to metal hydride discovery [31].

In this work, we develop ML models to predict the hydrogen sorption properties of Zr–Ti-based C14 Laves phase AB_2 alloys from their chemical composition. Two categories of input features are systematically compared: (i) element atomic percent variables, which directly encode the alloy composition, and (ii) properties-based variables derived from the composition,

including molar mass, bulk density, molar volume, atomic radius ratio, bulk modulus, electron density, and B/A ratio. Five ML algorithms—multivariate linear regression, random forest regression, ridge regression, k-nearest neighbour (KNN), and extreme gradient boosting (XGBoost)—are evaluated for their predictive performance. Forward feature selection is employed to identify the most informative feature subsets, and model performance is rigorously assessed using train, test, and cross-validation metrics.

2. Methodology

2.1. Dataset construction

Databases for this research were collected from previous work on AB_2 alloy-type compounds published in academic journals. This literature provides a stoichiometric analysis of constituent elements, phase abundance, and volume of C14 and C15 Laves phases, as well as the energy and entropy of hydrogen absorption. The initial dataset comprised 276 entries. After removing 16 entries for which only the C15 Laves phase was identified (out of 260 entries with phase identification data), and subsequently applying a variance filter to remove elements with variance lower than 0.0002, the final dataset contained 244 entries.

Figure 1 shows a heat map that indicates the frequency of each element used in an AB_2 intermetallic compound. Zr and Mn were the most used elements in the AB_2 intermetallic compound system. The collected variables were divided into independent and dependent variables. The independent variables were grouped into properties-based and element atomic percent-based variables of the alloy. The properties-based variables included molar

mass (MM), bulk density (BD), molar volume (MV), atomic radius ratio (RR), bulk modulus (BM), electron density (e/a), and the ratio between A-site components (Ti and Zr) and B-site components (B/A). Properties-based variables were calculated from available data in journals. The dependent variables were the volume of the C14 Laves phase (V14), enthalpy of hydrogen absorption (ΔH), entropy of hydrogen absorption (ΔS), and equilibrium plateau pressure (P_{eq}). At this stage, 276 lines of data were collected.

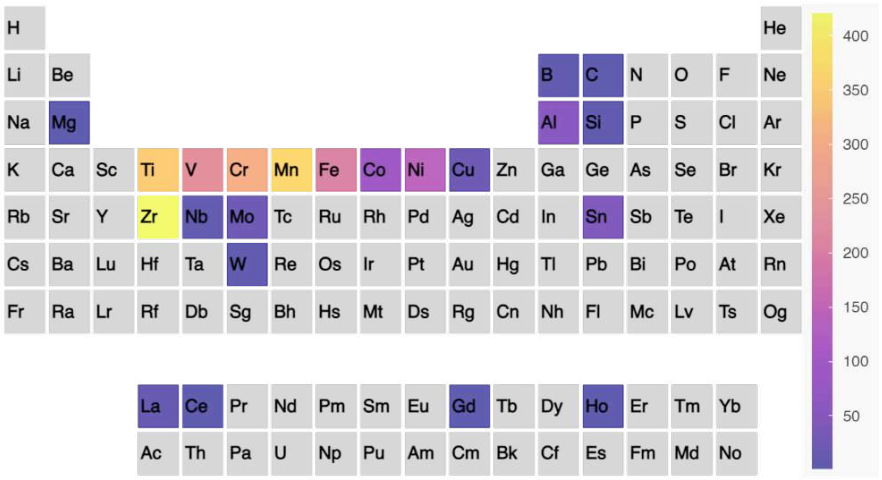


Figure 1: Heat map of element frequency in AB_2 intermetallic compounds from the compiled dataset. Zr and Mn are the most prevalent elements.

2.2. Data preprocessing

Before processing with machine learning, the dataset needed to be cleaned. Of the 276 entries collected, only 260 had phase identification data, and of these only 16 were C15 Laves phase entries; therefore, C15 entries were removed from the dataset, reducing it to 244 entries. A variance test was then conducted: elements with a variance lower than 0.0002 were filtered out. The

removed elements included Ho, Sn, Al, C, Mg, Gd, B, Mo, W, La, Si, Nb, and Ce. Next, the dataset was divided into four dependent variable groups: V14, ΔH, ΔS, and P_{eq}. The data distribution for each group is shown in Figure 2.

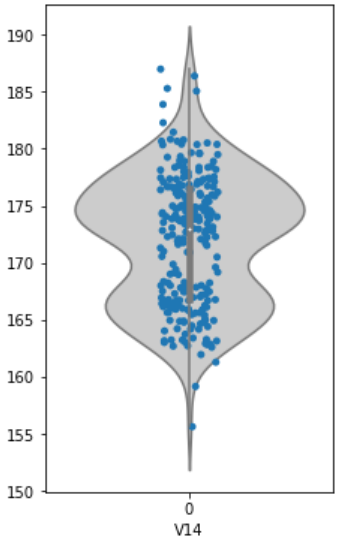
Using Pearson correlation, parameters that had a linear relationship were eliminated. Referring to [29], the linear correlation limit between parameters was 0.9. As shown in Figures 3 and 4, only Ti and Zr had a linear relationship greater than 0.9. Ti and Zr have a remarkably high correlation, possibly due to the interchangeability of Ti with Zr in the A site. The Zr value will automatically decrease when the Ti value increases, resulting in a high correlation value as shown by the dark red colour on the upper-left corner of the heat map. However, despite their high correlation, Ti and Zr were not eliminated from the dataset because of the considerable effect of Ti/Zr as the A-site elements on AB_2 properties. The dataset was scaled using Min–Max scaling, which transforms the data to a range of 0 to 1:

$$x_{\mathrm{scaled}} = \frac{x - x_{\mathrm{min}}}{x_{\mathrm{max}} - x_{\mathrm{min}}} \tag{1}$$

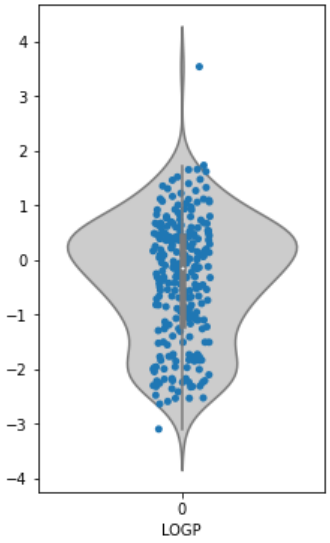
where x is the original feature value, and x_{min} and x_{max} are the minimum and maximum values of the feature, respectively.

2.3. Feature selection

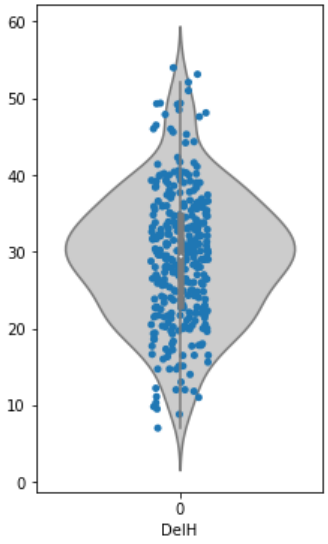
Before creating the model using machine learning, forward feature selection was conducted to identify the most important set of independent variables that could accurately predict the output variable. The algorithm used in the feature selection process adapted the model algorithm used later in model training. As shown in Figure 5, forward feature selection started



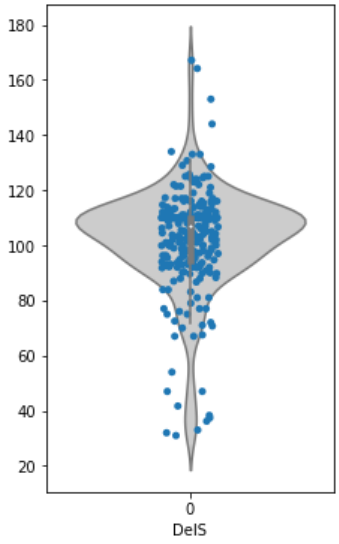
(a) V14



(b) ΔH



(c) ΔS



(d) P_{eq}

Figure 2: Data distribution of the four dependent variables: (a) V14, (b) ΔH, (c) ΔS, and (d) P_{eq}.

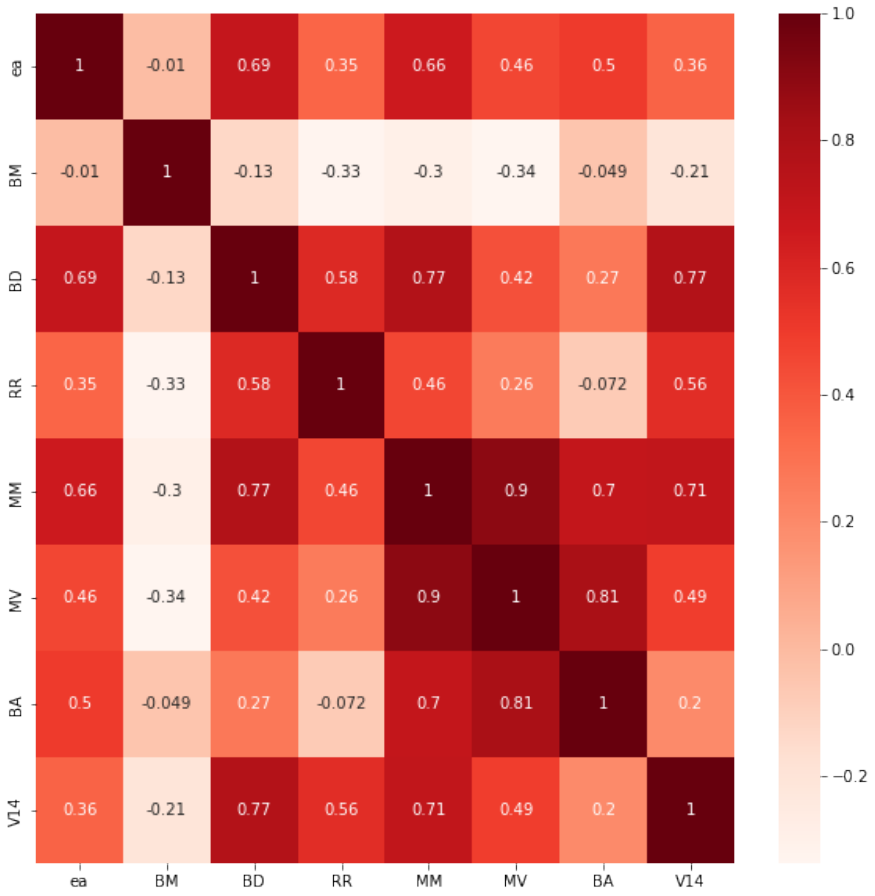


Figure 3: Pearson correlation heatmap for properties-based independent variables.

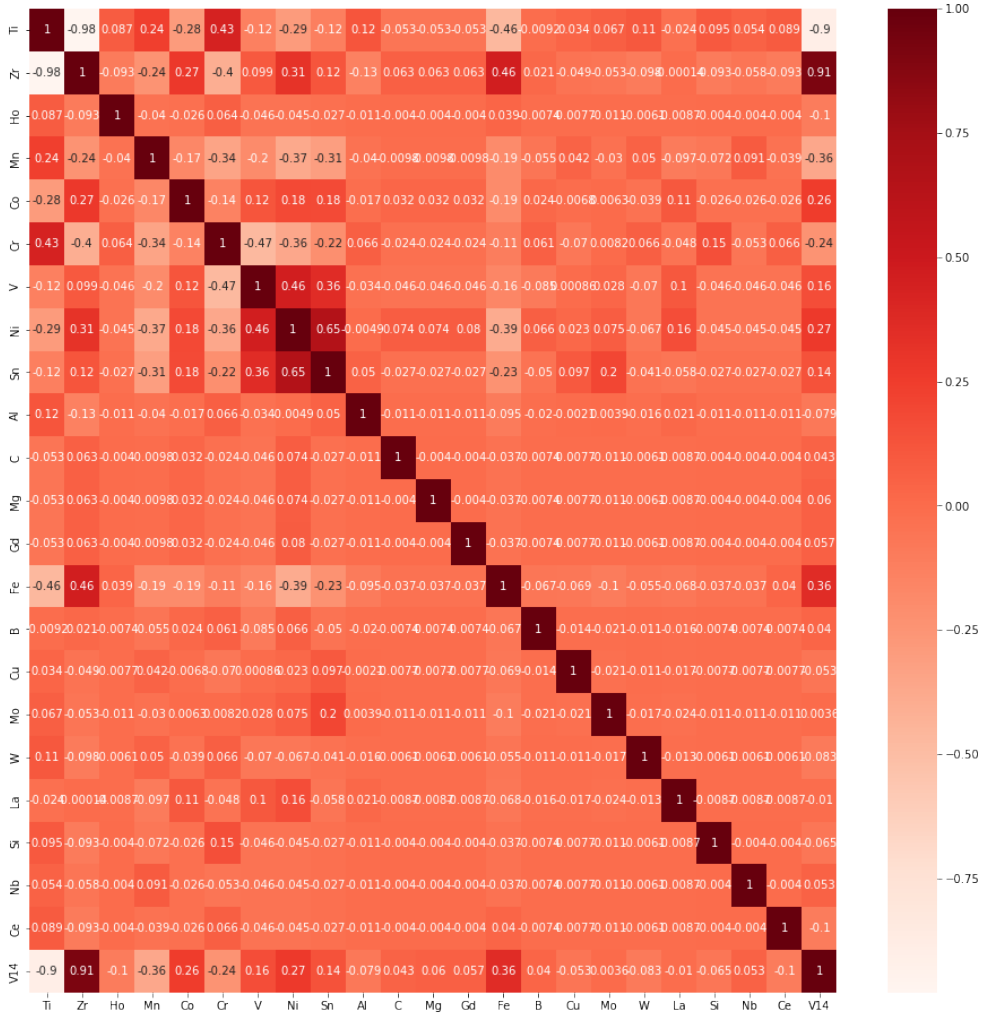


Figure 4: Pearson correlation heatmap for element atomic percent independent variables. The high correlation between Ti and Zr is visible in the upper-left corner.

with an empty feature set, iterated through the various features, and selected the one that maximized the accuracy. The features selected for each model algorithm varied depending on the model and dependent variable predicted.

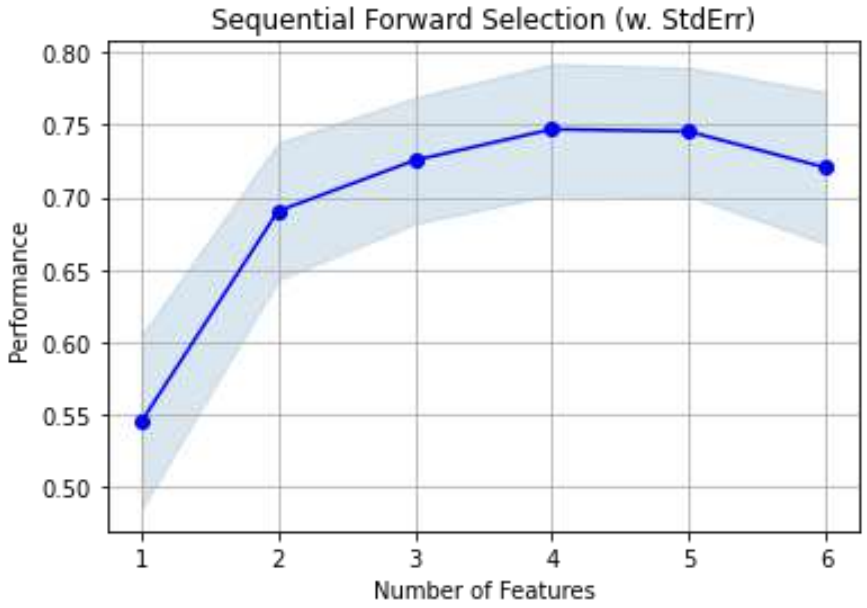


Figure 5: Example of forward feature selection result, showing the incremental improvement in model accuracy as features are sequentially added.

2.4. Machine learning algorithms

Five machine learning algorithms were used in this study:

- *Multivariate linear regression (LR)*: A linear approach that models the relationship between the independent variables and the dependent variable by fitting a linear equation to the observed data.
- *Random forest regression (RF)*: An ensemble learning method that constructs multiple decision trees during training and outputs the mean

prediction of the individual trees, reducing variance and improving generalization.

- *Ridge regression*: A regularized variant of linear regression that adds an L_2 penalty term to the loss function, shrinking coefficient estimates and reducing model variance, particularly useful when multicollinearity is present.

- *k-Nearest neighbour (KNN)*: A non-parametric, instance-based learning method that predicts the target value by averaging the responses of the k nearest training examples in the feature space. The optimal k value was determined through cross-validation.

- *Extreme gradient boosting (XGBoost)*: A gradient-boosted decision tree algorithm that builds an ensemble of weak learners sequentially, with each new tree correcting the residual errors of the previous ensemble.

2.5. Model training and evaluation

After feature selection, the selected parameters were split into independent (X) and dependent (Y) variables. The dataset was partitioned into a training set (80%) and a testing set (20%). The training set was used to train the model, while the testing set served as an independent evaluation of generalization performance. Cross-validation was conducted to avoid overfitting. Five-fold cross-validation (CV) was applied: the system automatically split the data into 5 subsets randomly and iteratively fitted the model with 4 subsets and evaluated on the remaining subset. The accuracies were averaged over the entire process and defined as the CV accuracy, reported as the validation set performance.

Three evaluation metrics were used: coefficient of determination (R^2), mean absolute error (MAE), and root mean squared error (RMSE). The train set score was obtained based on the difference between the predicted values from the X train dataset and the y train dataset. The test set scores were obtained from the difference between predicted values from the X test dataset and the y test dataset.

3. Results and discussion

This research used two types of independent variable—the element atomic percent of the alloy and the properties of each alloy—with the dependent variables V14, ΔH, ΔS, and P_{eq}. For V14, machine learning produced high accuracies, with element atomic percent variables presenting more accurate models than properties-based variables. For ΔH, both element atomic percent and properties-based variables produced moderate accuracies. For ΔS, both types produced low accuracies. For P_{eq}, both types produced moderate accuracies, and P_{eq} showed a linear correlation with V14.

3.1. Prediction of V14 from properties-based variables

Table 1 presents the ML prediction results for V14 using properties-based independent variables. Among the five algorithms, RF achieved the highest test set R^2 of 0.931, followed by KNN (k=5) at 0.889 and XGBoost at 0.882. Linear regression and ridge regression yielded substantially lower test accuracies (R^2 = 0.670 and 0.600, respectively), indicating that the relationship between properties-based features and V14 is not well captured by linear models alone.

Table 1: Machine learning results for V14 with properties-based independent variables.

Model	R^2			MAE (Å^3)			RMSE (Å^3)		
	Train	Test	Val	Train	Test	Val	Train	Test	Val
LR	0.746	0.670	0.715	1.999	2.675	2.059	2.747	3.621	2.810
RF	0.980	0.931	0.863	0.485	1.155	1.347	0.777	1.647	1.984
Ridge	0.722	0.600	0.702	2.120	2.896	2.193	2.870	3.987	2.914
KNN (k=5)	0.886	0.889	0.830	1.224	1.606	1.562	1.841	2.102	2.198
XGBoost	0.999	0.882	0.823	0.023	1.513	1.557	0.089	2.164	2.229

Note: Selected features — LR: e/a, BD, MV, B/A; RF: e/a, BD, RR, MV; Ridge: e/a, BD, RR, MV; KNN: RR, MM, MV; XGBoost: e/a, RR, MV, B/A. Val = 5-fold cross-validation.

Notably, XGBoost achieved a near-perfect training R^2 of 0.999, but its validation R^2 dropped to 0.823, and the RMSE increased from 0.089 (train) to 2.229 (validation), indicating mild overfitting. In contrast, RF exhibited better generalization, with a validation R^2 of 0.863 and a smaller gap between training and validation RMSE.

3.2. Prediction of ΔH from properties-based variables

Table 2 presents the ML prediction results for ΔH using properties-based independent variables. The prediction of enthalpy proved more challenging than V14. The best validation R^2 was 0.561 (RF), while LR and Ridge yielded R^2 values around 0.34–0.36, indicating that only about half of the variance in ΔH is captured by the models at best.

The moderate accuracies for ΔH prediction may be attributed to the

Table 2: Machine learning results for ΔH with properties-based independent variables.

Model	R^2			MAE (kJ/mol H_2)			RMSE (kJ/mol H_2)		
	Train	Test	Val	Train	Test	Val	Train	Test	Val
LR	0.381	0.290	0.360	4.874	6.254	4.916	6.639	7.972	6.714
RF	0.920	0.421	0.561	1.660	5.711	3.941	2.375	7.201	5.519
Ridge	0.364	0.262	0.336	4.962	6.449	5.035	6.730	8.129	6.839
KNN (k=3)	0.803	0.395	0.558	2.617	5.467	3.968	3.745	7.362	5.586
XGBoost	0.969	0.410	0.494	0.530	5.618	4.158	1.476	7.265	5.967

Note: Selected features — LR: e/a, BM, RR, MV; RF: e/a, BM, RR; Ridge: e/a, BM, RR, MV; KNN: e/a, BM, BD, RR; XGBoost: e/a, BM, RR. Val = 5-fold cross-validation.

complex interplay of electronic, structural, and vibrational factors that govern the enthalpy of hydrogen absorption, which are not fully captured by the relatively coarse properties-based descriptors.

3.3. Prediction of ΔS from properties-based variables

Table 3 presents the ML prediction results for ΔS using properties-based independent variables. The prediction of entropy proved to be the most challenging task, with validation R^2 values being negative for most algorithms, indicating that the models perform worse than simply predicting the mean value. Even the best-performing algorithm (KNN, validation $R^2 = 0.144$) captured very little of the variance in ΔS.

This outcome is not unexpected, as the entropy of hydrogen absorption is governed by configurational, vibrational, and electronic contributions that

Table 3: Machine learning results for ΔS with properties-based independent variables.

Model	R^2			MAE (J/mol H_2/K)			RMSE (J/mol H_2/K)		
	Train	Test	Val	Train	Test	Val	Train	Test	Val
LR	0.066	0.104	−0.146	12.797	12.795	13.273	18.187	17.745	18.938
RF	0.866	0.499	−0.012	4.304	9.490	11.396	6.880	13.264	17.762
Ridge	0.065	0.097	−0.112	12.761	12.769	13.142	18.205	17.814	18.766
KNN (k=5)	0.463	0.196	0.144	9.118	12.916	11.573	13.794	16.806	16.655
XGBoost	0.964	0.378	−0.313	1.008	10.656	19.484	3.558	14.787	12.353

Note: Selected features — LR: e/a, B/A; RF: e/a, BM, MV, B/A; Ridge: e/a, B/A; KNN: BD, RR; XGBoost: e/a, BM, MV, B/A. Val = 5-fold cross-validation.

are highly sensitive to local structural details and temperature-dependent phenomena not captured by static bulk property descriptors.

3.4. Prediction of P_{eq} from properties-based variables

Table 4 presents the ML prediction results for P_{eq} using properties-based independent variables. The equilibrium pressure exhibited moderate prediction accuracies. RF achieved the highest validation R^2 of 0.718, while LR yielded the highest test R^2 of 0.658.

3.5. Prediction of V14 from element atomic percent variables

Table 5 presents the ML prediction results for V14 using element atomic percent independent variables. The prediction accuracy improved considerably compared to properties-based features. Linear regression achieved a remarkable test R^2 of 0.955—a substantial improvement over its properties-based counterpart (0.670). This result demonstrates that the element com-

Table 4: Machine learning results for P_{eq} with properties-based independent variables.

Model	R^2			MAE (atm)			RMSE (atm)		
	Train	Test	Val	Train	Test	Val	Train	Test	Val
LR	0.593	0.658	0.557	0.571	0.508	0.588	0.704	0.684	0.728
RF	0.954	0.636	0.718	0.169	0.410	0.421	0.238	0.707	0.581
Ridge	0.571	0.533	0.538	0.588	0.574	0.605	0.722	0.800	0.745
KNN (k=3)	0.865	0.602	0.689	0.291	0.434	0.441	0.406	0.739	0.605
XGBoost	0.984	0.616	0.690	0.042	0.419	0.416	0.138	0.726	0.609

Note: Selected features — LR: BM, BD, RR, MV; RF: BM, BD, RR, MV; Ridge: BM, BD, RR, MV; KNN: e/a, RR, MM; XGBoost: B/A, e/a, RR, MV. Val = 5-fold cross-validation.

position encodes more direct and informative signals for predicting V14 than the derived physical properties.

Interestingly, while XGBoost again achieved near-perfect training accuracy ($R^2 = 0.998$), its test and validation R^2 values (0.838 and 0.835) were lower than those of the simpler linear regression model, suggesting overfitting. The observation that a simple linear model outperforms complex ensemble methods implies that the element atomic percent features exhibit a predominantly linear relationship with V14.

3.6. Prediction of ΔH from element atomic percent variables

Table 6 presents the ML prediction results for ΔH using element atomic percent independent variables. As with properties-based features, the prediction of enthalpy remained challenging. The best validation R^2 was 0.531

Table 5: Machine learning results for V14 with element atomic percent independent variables.

Model	R^2			MAE (Å^3)			RMSE (Å^3)		
	Train	Test	Val	Train	Test	Val	Train	Test	Val
LR	0.927	0.955	0.911	0.952	0.999	1.026	1.468	1.329	1.548
RF	0.940	0.898	0.795	0.621	1.318	1.454	1.332	2.012	2.409
Ridge	0.895	0.893	0.876	1.182	1.534	1.285	1.763	2.055	1.862
KNN (k=2)	0.953	0.876	0.850	0.761	1.455	1.388	1.177	2.221	2.064
XGBoost	0.998	0.838	0.835	0.084	1.496	1.256	0.220	2.539	2.152

Note: Selected features — LR: Ti, Zr, Mn, Co, Cr, V, Ni, Sn, Al, Fe; RF: Ti, Zr, Co, Cr, V, Ni, Sn, Al, Fe; Ridge: Ti, Zr, Mn, Co, Cr, V, Ni, Sn, Al, Fe; KNN: Ti, Zr, Mn, Cr, Sn, Al; XGBoost: Ti, Zr, Mn, Co, V, Ni, Sn, Al, Fe. Val = 5-fold cross-validation.

(KNN), and the best test R^2 was only 0.413 (KNN), indicating that element composition alone does not fully capture the factors governing enthalpy.

3.7. Prediction of ΔS from element atomic percent variables

Table 7 presents the ML prediction results for ΔS using element atomic percent independent variables. As with properties-based features, the prediction of entropy was the most challenging task, with validation R^2 values being negative for most algorithms. The best validation R^2 was only 0.218 (KNN).

3.8. Prediction of P_{eq} from element atomic percent variables

Table 8 presents the ML prediction results for P_{eq} using element atomic percent independent variables. The equilibrium pressure exhibited moderate

Table 6: Machine learning results for ΔH with element atomic percent independent variables.

Model	R^2			MAE (kJ/mol H_2)			RMSE (kJ/mol H_2)		
	Train	Test	Val	Train	Test	Val	Train	Test	Val
LR	0.365	0.252	0.349	4.756	6.422	4.805	6.720	8.183	6.772
RF	0.609	0.262	0.410	3.136	6.027	4.572	5.274	8.129	6.483
Ridge	0.362	0.247	0.347	4.788	6.441	4.839	6.738	8.210	6.784
KNN (k=4)	0.705	0.413	0.531	3.172	5.175	4.166	4.585	7.254	5.742
XGBoost	0.832	0.329	0.507	1.502	5.732	4.201	3.463	7.750	5.844

Note: Selected features — LR: Zr, Al, Fe; RF: Ti, Cr; Ridge: Zr, Al, Fe; KNN: Ti, Zr, Ni, Sn, Al, Fe; XGBoost: Ti, Mn, Cr, Ni, Sn. Val = 5-fold cross-validation.

Table 7: Machine learning results for ΔS with element atomic percent independent variables.

Model	R^2			MAE (J/mol H_2/K)			RMSE (J/mol H_2/K)		
	Train	Test	Val	Train	Test	Val	Train	Test	Val
LR	0.007	−0.028	−0.068	12.594	13.682	12.817	18.761	19.013	18.646
RF	0.628	0.316	0.122	5.791	10.373	10.446	11.487	15.499	16.460
Ridge	0.006	−0.022	−0.067	12.575	13.644	12.770	18.765	18.962	18.640
KNN (k=6)	0.533	0.342	0.218	8.210	10.611	10.266	12.868	15.203	15.773
XGBoost	0.664	0.130	−0.020	4.278	11.825	10.994	10.907	17.478	18.038

Note: Selected features — LR: Al; RF: Zr, Mn, Ni, Sn, Al; Ridge: Al; KNN: Zr, Mn, Cr, V, Sn, Al, Fe; XGBoost: Zr, Mn, Ni, Sn. Val = 5-fold cross-validation.

prediction accuracies across all algorithms. Linear regression achieved the highest test R^2 of 0.741, while KNN (k=4) and XGBoost yielded the highest validation R^2 of 0.739.

Table 8: Machine learning results for P_{eq} with element atomic percent independent variables.

Model	R^2			MAE (atm)			RMSE (atm)		
	Train	Test	Val	Train	Test	Val	Train	Test	Val
LR	0.697	0.741	0.675	0.471	0.394	0.486	0.604	0.555	0.622
RF	0.911	0.613	0.721	0.228	0.377	0.430	0.328	0.677	0.575
Ridge	0.635	0.693	0.619	0.516	0.471	0.530	0.664	0.603	0.673
KNN (k=4)	0.845	0.688	0.739	0.321	0.396	0.424	0.432	0.609	0.555
XGBoost	0.945	0.707	0.739	0.111	0.339	0.397	0.257	0.589	0.555

Note: Selected features — LR: Ti, Zr, Co, V, Ni, Al, Fe; RF: Ti, Zr, Co, Ni, Fe; Ridge: Zr, Co, V, Al, Fe; KNN: Ti, Zr, Co, Cr, Ni, Al, Fe; XGBoost: Zr, Co, V, Ni, Sn, Fe. Val = 5-fold cross-validation.

A notable finding is the linear correlation observed between P_{eq} and V14, as illustrated in Figure 6. This relationship is physically meaningful: the equilibrium pressure of hydrogen absorption in AB_2 alloys is thermodynamically linked to the unit cell volume through the van't Hoff equation, where larger interstitial sites (associated with larger V14) generally provide more favourable sites for hydrogen occupation, thereby lowering the equilibrium pressure.

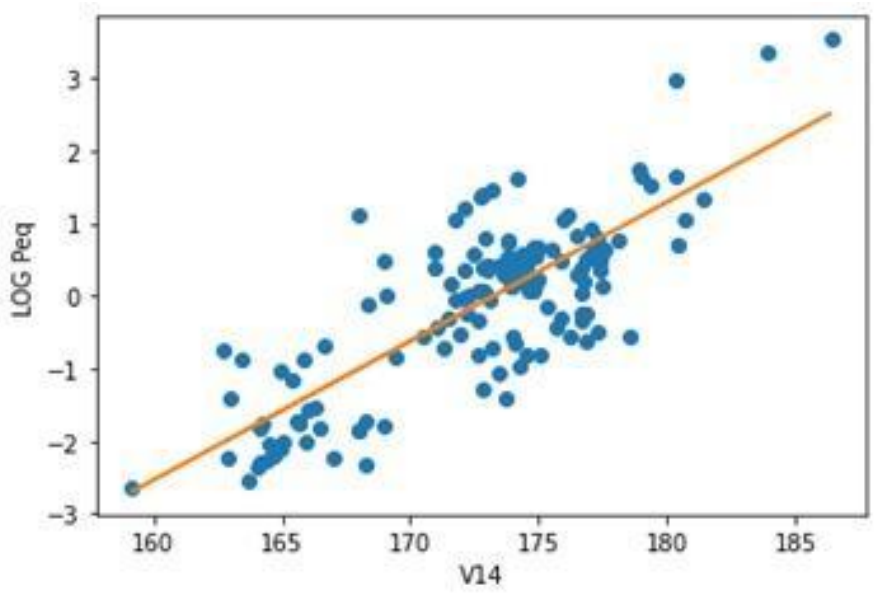


Figure 6: Correlation between equilibrium pressure (P_{eq}) and C14 unit cell volume (V14).

3.9. Visualization of prediction results

The visualization of V14 test set predictions with the five machine learning methods is shown in Figure 7 for element atomic percent-based features and Figure 8 for properties-based features.

3.10. Comparison of feature types and algorithms

A comparative analysis of the two feature types reveals a clear trend: element atomic percent variables consistently outperform properties-based variables for the prediction of V14. The element-based features provide a more direct and granular representation of the alloy composition, enabling the models to capture composition-dependent variations in the C14 unit cell volume with greater fidelity. In contrast, the properties-based variables, while physically interpretable, represent aggregated descriptors that may obscure

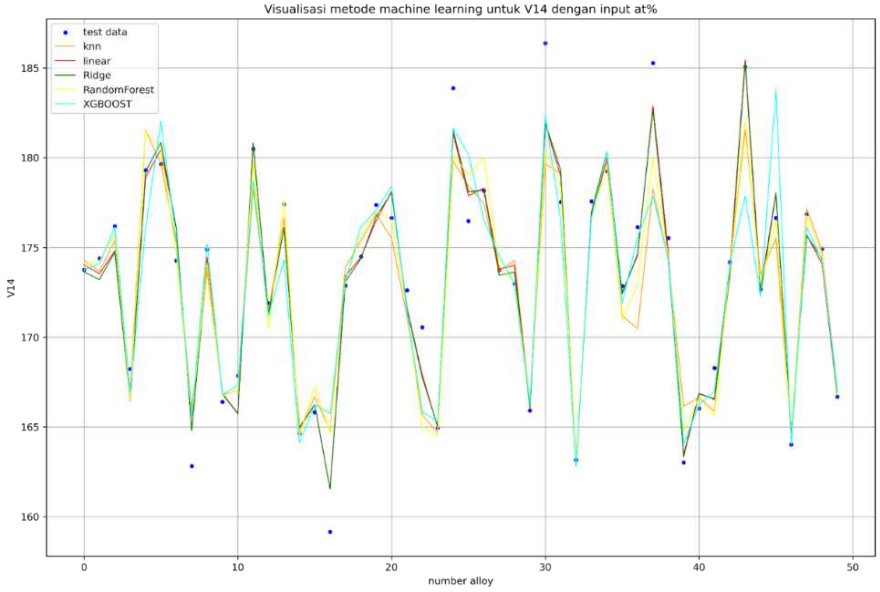


Figure 7: Prediction of V14 using element atomic percent variables: (a) linear regression, (b) random forest, (c) ridge regression, (d) KNN, and (e) XGBoost. Predicted vs. experimental values are shown for training, testing, and validation sets.

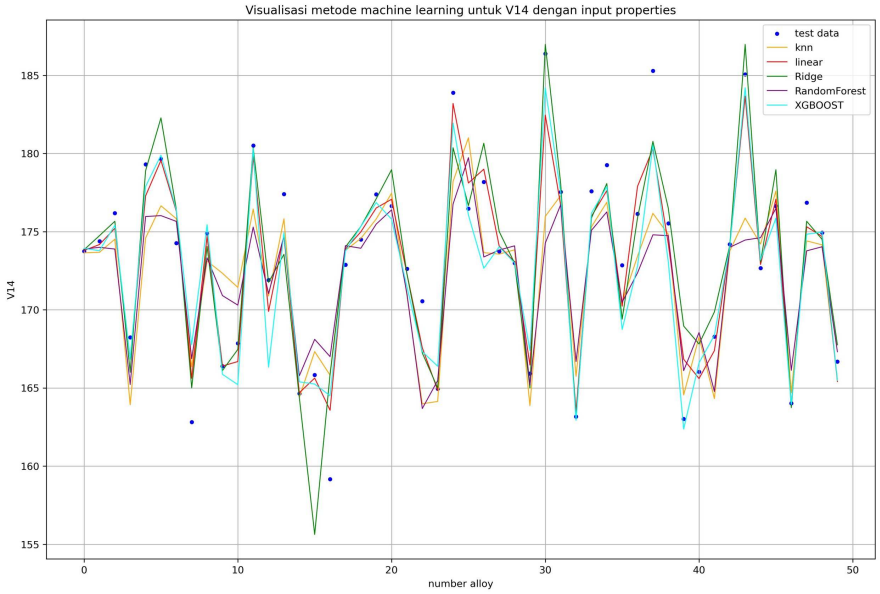


Figure 8: Prediction of V14 using properties-based variables: (a) linear regression, (b) random forest, (c) ridge regression, (d) KNN, and (e) XGBoost. Predicted vs. experimental values are shown for training, testing, and validation sets.

element-specific contributions.

For V14 prediction with element-based features, linear regression unexpectedly achieved the best test set performance ($R^2 = 0.955$), surpassing more complex algorithms. This finding indicates that the relationship between element composition and V14 is predominantly linear, likely because the unit cell volume is primarily determined by the weighted average of the atomic radii of the constituent elements.

For ΔH and ΔS, neither feature type yielded satisfactory prediction accuracies, highlighting opportunities for more advanced feature engineering to capture electronic and vibrational contributions to the thermodynamic properties. For P_{eq}, the moderate accuracies achieved with element-based features are encouraging and suggest that improvements in feature engineering could lead to more reliable predictions.

Table 9 summarises the best-performing algorithm for each target variable and feature type, ranked by validation R^2. Across all four dependent variables, element atomic percent features consistently matched or outperformed properties-based features, and the best algorithm varied by target: linear regression for V14, KNN for ΔH and ΔS, and KNN/XGBoost for P_{eq}.

4. Conclusions

This study demonstrated the application of machine learning to predict the hydrogen sorption properties of Zr–Ti-based C14 Laves phase AB_2 alloys from their chemical composition. A curated dataset of 244 alloys was used to train and evaluate five ML algorithms—linear regression, random forest, ridge regression, KNN, and XGBoost—using both properties-based

Table 9: Summary of best-performing models by target variable and feature type, ranked by validation R^2.

Target	Best algorithm	R^2		
		Train	Test	Val
Properties-based features				
V14	RF	0.980	0.931	0.863
ΔH	RF	0.920	0.421	0.561
ΔS	KNN (k=5)	0.463	0.196	0.144
P_{eq}	RF	0.954	0.636	0.718
Element atomic percent features				
V14	LR	0.927	0.955	0.911
ΔH	KNN (k=4)	0.705	0.413	0.531
ΔS	KNN (k=6)	0.533	0.342	0.218
P_{eq}	KNN/XGB	0.845/0.945	0.688/0.707	0.739/0.739

and element atomic percent input features. The principal findings are as follows:

1. Element atomic percent variables outperform properties-based features for the prediction of V14, with linear regression achieving the highest test R^2 of 0.955 using element-based features.
2. No good correlation was found between either type of feature and ΔH. The best validation R^2 for ΔH was only 0.561 (RF, properties-based) and 0.531 (KNN, element-based), indicating that more advanced feature engineering could improve these predictions.
3. ΔS prediction proved the most challenging, with most models yielding negative validation R^2 values for both feature types, indicating that the current descriptors are insufficient to capture the configurational, vibrational, and electronic contributions governing entropy.
4. P_{eq} showed the strongest correlation with fundamental properties among the thermodynamic variables, with a notable linear correlation with V14. Element-based features achieved a test R^2 of up to 0.741 and a validation R^2 of 0.739.
5. Forward feature selection effectively identified compact yet informative feature subsets, with the selected features varying across algorithms and target variables.

These results are summarised in Table 9 and demonstrate that ML can effectively predict structural properties (V14) of AB_2 alloys from composition alone, while thermodynamic properties (ΔH, ΔS, P_{eq}) present opportunities for more advanced feature engineering to achieve reliable prediction.

CRediT authorship contribution statement

S. Suwarno: Conceptualization, Methodology, Supervision, Writing – review & editing. **M. Ismail**: Resources, Writing – review & editing. **Witantyo**: Data curation, Software, Investigation, Writing – original draft. **I. Tolj**: Writing – review & editing.

Declaration of competing interest

The authors declare that they have no known competing financial interests or personal relationships that could have appeared to influence the work reported in this paper.

Data availability

All data supporting the findings of this study are available within the paper and its Supplementary Information.

Acknowledgements

This research is funded by the Indonesian Endowment Fund for Education (LPDP) on behalf of the Indonesian Ministry of Higher Education, Science and Technology and managed under the EQUITY Program (Contract No. 4299/B3/DT.03.08/2025 & No 3029/PKS/ITS/2025).

References

[1] Züttel, A., 2003. Materials for hydrogen storage. Materials Today 6, 24–33. https://doi.org/10.1016/S1369-7021(03)00922-4

[2] Yartys, V., Noreus, D., Latroche, M., 2016. Metal hydrides as negative electrode materials for Ni–MH batteries. Applied Physics A 122, 43. https://doi.org/10.1007/s00339-015-9538-9

[3] Suwarno, S., Solberg, J.K., Mæhlen, J.P., Denys, R.V., Krogh, B., Ochoa-Fernández, E., et al., 2013. Non-isothermal kinetics and in situ SR XRD studies of hydrogen desorption from dihydrides of binary Ti–V alloys. International Journal of Hydrogen Energy 38, 14704–14714. https://doi.org/10.1016/j.ijhydene.2013.08.103

[4] Suwarno, S., Solberg, J.K., Mæhlen, J.P., Krogh, B., Yartys, V.A., 2014. The effects of rapid solidification on microstructure and hydrogen sorption properties of binary BCC Ti–V alloys. Journal of Alloys and Compounds 582, 540–546. https://doi.org/10.1016/j.jallcom.2013.08.077

[5] Mungole, M.N., Balasubramanian, R., 1998. Hydrogen solubility in Zr based AB_2 alloys. International Journal of Hydrogen Energy 23, 349–353. https://doi.org/10.1016/S0360-3199(97)00064-2

[6] Ouellette, R.J., Rawn, J.D., 2020. Laves phases: C14, C15, and C36 structures. In: Intermetallic Compounds, pp. 215–241. https://doi.org/10.1016/B978-0-12-8198-6.00008-2

[7] Suwarno, S., Ismail, M., 2016. Kinetic and thermodynamic studies of hydrogen sorption in AB_2-type alloys. International Journal of Hydrogen Energy 41, 13105–13113. https://doi.org/10.1016/j.ijhydene.2016.05.289

[8] Young, K., Ouchi, T., Huang, B., Fetcenko, M.A., 2008. Structure and hydrogen storage properties of C14 Laves phase alloys. Journal of Alloys and Compounds 466, 296–302. https://doi.org/10.1016/j.jallcom.2007.06.023

[9] Young, K.-H., Koch, J., Wan, C., Denys, R., Yartys, V., 2017. Cell performance comparison between C14- and C15-predominated AB_2 metal hydride alloys. Batteries 3, 29. https://doi.org/10.3390/batteries3040029

[10] Hu, J., Li, H., Zhang, Z., 2017. Hydrogen storage properties of Zr-based AB_2 Laves phase alloys for nickel-metal hydride batteries. Journal of Power Sources 362, 42–48. https://doi.org/10.1016/j.jpowsour.2017.07.012

[11] Ulmer, U., Asano, K., Bergfeldt, T., Chakravadhanula, V.S.K., Dittmeyer, R., Enoki, H., et al., 2014. Effect of oxygen on the microstructure and hydrogen storage properties of V–Ti–Cr–Fe quaternary solid solutions. International Journal of Hydrogen Energy 39, 20000–20008. https://doi.org/10.1016/j.ijhydene.2014.08.152

[12] Santos, S.F., Huot, J., 2009. Hydrogen storage in $TiCr_{1.2}(FeV)_x$ BCC solid solutions. Journal of Alloys and Compounds 472, 247–251. https://doi.org/10.1016/j.jallcom.2008.04.062

[13] Liu, Y., Zhao, T., Ju, W., Shi, S., 2017. Materials discovery and design using machine learning. Journal of Materiomics 3, 159–177. https://doi.org/10.1016/j.jmat.2017.08.002

[14] Schmidt, J., Marques, M.R.G., Botti, S., Marques, M.A.L., 2019. Recent advances and applications of machine learning in solid-state materials science. npj Computational Materials 5, 1–36. https://doi.org/10.1038/s41524-019-0221-0

[15] Correa-Baena, J.-P., Hippalgaonkar, K., van Duren, J., Jaffer, S., Chandrasekhar, V.R., Stevanovic, V., et al., 2018. Accelerating materials development via automation, machine learning, and high-performance computing. Joule 2, 1410–1420. https://doi.org/10.1016/j.joule.2018.05.009

[16] Witman, M., Ling, S., Grant, D.M., Walker, G.S., Agarwal, S., Stavila, V., Allendorf, M.D., 2020. Extracting an empirical intermetallic hydride design principle from limited data via interpretable machine learning. Journal of Physical Chemistry Letters 11, 40–47. https://doi.org/10.1021/acs.jpclett.9b02971

[17] Ward, L., Agrawal, A., Choudhary, A., Wolverton, C., 2016. A general-purpose machine-learning framework for predicting properties of inorganic materials. npj Computational Materials 2, 16028. https://doi.org/10.1038/npjcompumats.2016.28

[18] Rahnama, A., Zepon, G., Sridhar, S., 2019. Machine learning based prediction of metal hydrides for hydrogen storage, part I: Prediction of hydrogen weight percent. International Journal of Hydrogen Energy 44, 7337–7344. https://doi.org/10.1016/j.ijhydene.2019.01.261

[19] Rahnama, A., Zepon, G., Sridhar, S., 2019. Machine learning based

prediction of metal hydrides for hydrogen storage, part II: Prediction of material class. International Journal of Hydrogen Energy 44, 7345–7353. https://doi.org/10.1016/j.ijhydene.2019.01.264

[20] Zhong, X., Yu, H., Wang, J., Cui, S., 2022. Machine learning-driven discovery of AB_2-type hydrogen storage alloys. Journal of Materials Chemistry A 10, 1523–1535. https://doi.org/10.1039/D1TA09756A

[21] Li, H., Zhang, Z., Hu, J., Cheng, H., 2021. Data-driven prediction of hydrogen storage properties in AB_2 intermetallic compounds. International Journal of Hydrogen Energy 46, 35256–35267. https://doi.org/10.1016/j.ijhydene.2021.08.056

[22] Kim, J.M., Ha, T., Lee, J., Lee, Y.S., Shim, J.H., 2023. Prediction of pressure-composition-temperature curves of AB_2-type hydrogen storage alloys by machine learning. Metals and Materials International 29, 861–869. https://doi.org/10.1007/s12540-022-01262-0

[23] Suwarno, S., Dicky, G., Suyuthi, A., Effendi, M., Witantyo, W., Noerochim, L., Ismail, M., 2022. Machine learning analysis of alloying element effects on hydrogen storage properties of AB_2 metal hydrides. International Journal of Hydrogen Energy 47, 11938–11947. https://doi.org/10.1016/j.ijhydene.2022.01.210

[24] Maghsoudy, S., Zakerabbasi, P., Baghban, A., Esmaeili, A., Habibzadeh, S., 2024. Connectionist technique estimates of hydrogen storage capacity on metal hydrides using hybrid GAPSO-LSSVM approach. Scientific Reports 14, 1503. https://doi.org/10.1038/s41598-024-52086-4

[25] Gheytanzadeh, M., Rajabhasani, F., Baghban, A., 2022. Estimating hydrogen absorption energy on different metal hydrides using Gaussian process regression approach. Scientific Reports 12, 21902. https://doi.org/10.1038/s41598-022-26522-2

[26] Chen, L., Wang, Z., Liu, Y., 2023. Random forest regression for predicting thermodynamic properties of hydrogen storage alloys. Computational Materials Science 218, 112008. https://doi.org/10.1016/j.commatsci.2023.112008

[27] Enblom, V., Clulow, R., Ha, T.-J., Witman, M.D., Way, L.E., Han, S.J., Carvalho, P.H.B.B., Stavila, V., Suh, J.-Y., Sahlberg, M., 2025. A combined experimental and machine learning exploration of $Ti_{2-x}Zr_xMnCrFeNi$ high entropy Laves hydrides. Materials Today 54, 107876. https://doi.org/10.1016/j.mattod.2025.107876

[28] Floriano, R., Edalati, P., Andrade, G., Strozi, R.B., Dangwal, S., Edalati, K., 2025. Room temperature hydrogen storage properties of Ti-Zr-Mn-Fe-Co high-entropy alloys designed by a combination of semi-empirical descriptors, thermodynamic calculations and machine learning. Journal of Alloys and Compounds 1010, 177835. https://doi.org/10.1016/j.jallcom.2024.177835

[29] Zhang, Z., Li, M., Flores, K., Mishra, R., 2020. Machine learning formation enthalpies of intermetallics. Journal of Applied Physics 128, 105103. https://doi.org/10.1063/5.0012323

[30] Jang, S.-H., Zhang, D., Jia, X., Tran, H.B., Zhang, L., Sato, R.,

Hashimoto, Y., Sato, T., Konno, K., Sato, S.-I., 2025. Digital hydrogen platform (DigHyd): A rigorously curated database for hydrogen storage materials empowered by AI-assisted literature mining. arXiv:2603.14139.

[31] Beltrame, G., Dematteis, E.M., Stavila, V., Rizzi, P., Baricco, M., 2025. Application of machine learning and data augmentation algorithms in the discovery of metal hydrides for hydrogen storage. Metals 15, 1221. https://doi.org/10.3390/met1511221

Supplementary Files

This is a list of supplementary files associated with this preprint. Click to download.

- Databasefinal.xlsx